LITHOS 516-517 (2025) 108285

Contents lists available at ScienceDirect

LITHOS

journal homepage: www.elsevier.com/locate/lithos

Emplacement of the Pindos ophiolite, NW Greece: P-T-t-kinematic constraints from the metamorphic sole

Dimitrios Moutzouris [a,*,1], Evangelos Moulas [a], Dimitrios Kostopoulos [b], Panagiotis Pomonis [b], Aratz Beranoaguirre [c], Elias Chatzitheodoridis [d], Axel Gerdes [c]

[a] *Institute of Geosciences and Mainz Institute of Multiscale Modeling (M^3ODEL), Johannes-Gutenberg University, Mainz, Germany*
[b] *Faculty of Geology and Geoenvironment, Department of Mineralogy and Petrology, National and Kapodistrian University of Athens, Athens, Greece*
[c] *Department of Geosciences and Frankfurt Isotope and Element Research Center (FIERCE), Goethe-University Frankfurt, Frankfurt am Main, Germany*
[d] *Department of Geological Sciences, School of Mining and Metallurgical Engineering, National Technical University of Athens, Athens, Greece*

A R T I C L E I N F O

Keywords:
Pindos ophiolite
ophiolite obduction
metamorphic sole
elastic barometry
thermobarometry

A B S T R A C T

Metamorphic soles are key petrotectonic units that offer valuable insights into the processes governing ophiolite emplacement on continental margins (obduction). In this work, we have investigated the metamorphic sole of the Pindos ophiolite in northwestern Greece. In the studied locality, the sole is sandwiched between mantle peridotites and pillow lavas of N-MORB affinity. Our study focuses on two lithologies from the metamorphic sole: a garnet-mica schist (metapelite) and a mafic amphibolite. Kinematic indicators from the garnet-mica schists are consistent with top-to-the-NE shearing of the Pindos ophiolite on the Pelagonian zone. Petrographic and textural evidence, geothermometry results (Fe—Mg garnet-biotite exchange and paragonite-muscovite solvus thermometry), and phase-equilibria modelling bracket the upper-limit of metamorphism at amphibolite-facies conditions (630 ± 20 °C and 1.1 ± 0.2GPa). Moreover, Quartz-in-Garnet (QuiG) barometry yields a pressure of ~1.2GPa for 630 °C demonstrating the equilibration of garnet inclusions at high-pressure conditions. New $^{40}Ar/^{39}Ar$ dating results from *syn*-kinematic muscovite from the metapelite and amphibole from the amphibolite indicate an apparent minimum age of 164.16 ± 0.37 Ma and a consistent age plateau at 165.5 ± 0.73 Ma respectively. Notably, the amphibole exhibits no evidence of argon loss. The muscovite age, by contrast, should be considered a minimum apparent age due to the potential influence of argon diffusion. Finally, U—Pb geochronology of garnet was dominated by inclusions and did not result in a meaningful age. The measured ages imply cooling rates for the Pindos metamorphic sole ranging from 60 to 625 °C/Ma.

1. Introduction

The obduction of ophiolites onto continental crust and the formation of metamorphic soles at the base of ophiolite sequences have been subjects of ongoing research for many years. Obduction is recognized as a complex thermomechanical phenomenon requiring the emplacement of large and dense segments of oceanic lithosphere onto continental crust (e.g., Dewey, 1976). Numerous theories have been proposed since, with most theories invoking an intra-oceanic subduction system as the emplacement mechanism of ophiolitic sequences onto continental margins (Hacker et al., 1996; Robertson, 2004). Others attribute the initiation of intra-oceanic subduction and later emplacement of an ophiolite to the collapse of a mid-ocean ridge (e.g., Boudier et al., 1985).

Regardless of the geodynamic setting, the obduction of an ophiolite sequence on the continental margin is commonly documented by the presence of high-grade metamorphic rocks, also referred to as metamorphic soles, that are characterized by mixed (oceanic and continental) affinities (e.g., Agard et al., 2016 and references therein). Metamorphic soles represent slivers of metamorphic rocks found beneath the basal mantle peridotites of ophiolitic complexes. They exhibit a range of metamorphic grades, spanning from greenschist- to amphibolite- and granulite-facies conditions. Notably, these rocks display an inverse metamorphic gradient. The metamorphic grade can reach granulite-facies conditions close to the contact with the overlying

* Corresponding author.
E-mail addresses: dmoutzou@uni-mainz.de (D. Moutzouris), evmoulas@uni-mainz.de (E. Moulas), dikostop@geol.uoa.gr (D. Kostopoulos), ppomonis@geol.uoa.gr (P. Pomonis), beranoaguirre@em.uni-frankfurt.de (A. Beranoaguirre), eliasch@metal.ntua.gr (E. Chatzitheodoridis), gerdes@em.uni-frankfurt.de (A. Gerdes).
[1] Postal address: Institute of Geosciences, University of Mainz, J.-J. Becher-Weg 21, Mainz, Germany

https://doi.org/10.1016/j.lithos.2025.108285
Received 2 June 2025; Received in revised form 23 September 2025; Accepted 1 October 2025
Available online 11 October 2025

peridotites (e.g., Myhill, 2011). The formation of metamorphic soles has in general been associated with an intra-oceanic thrusting system (e.g., Williams and Smyth, 1973) but the mechanics and the timescales of this process are generally poorly constrained.

To gain a deeper understanding of the pressure (*P*), temperature (*T*) and time (*t*) constraints of ophiolite obduction, we examined the Pindos metamorphic sole in northwestern Greece (Fig. 1A). Our study focused on the metamorphic conditions experienced by a metapelitic lithology within the sole. We provide thermobarometric and phase equilibria evidence of *syn*-kinematic recrystallization at upper amphibolite-facies metamorphism. Kinematic indicators from the sole metapelites point to a top-to-the NE sense of shearing. We obtained new $^{40}Ar/^{39}Ar$ apparent ages for metamorphic magnesio-hornblende from a sole amphibolite and syn-kinematic muscovite from the sole metapelite indicating that the metamorphic sole formed in middle Jurassic times. Moreover, we attempted to date garnet using U—Pb geochronology, but the presence of multiple zircon inclusions prevented us from obtaining a reliable growth age. The close correlation of our $^{40}Ar/^{39}Ar$ ages with the crystallization age of ophiolitic gabbros from Pindos (Liati et al., 2004) indicates tectono-metamorphic processes occurring within a specific time frame. Finally, the cooling ages of muscovite and amphibole suggest that the peak metamorphic conditions were followed by rapid cooling, indicative of fast transient processes during ophiolite emplacement.

2. Regional geology

Upper Palaeozoic plate reconstructions (e.g., Stampfli et al., 2013) show the northward subduction of the Palaeotethys oceanic tract beneath Laurasia (350–280 Ma), the southernmost margin of which was composed, among other blocks, of Adria, the Hellenides and Anatolia. Late Carboniferous magmatism in the Greek area is related to granitoid emplacement between 320 and 280 Ma (Anders et al., 2007 and references therein) and formation of the Pelagonian cordillera. This is the backbone of Greece stretching from the border with Albania in the northwest to the Cycladic archipelago in the southeast (Fig. 1A). Subsequent roll-back of the Palaeotethyan slab triggered the collapse of most of the European Variscan orogen. In the Triassic, extension in the upper plate led to the opening of oceanic marginal basins, younging southwards (Scythian to Anisian in the Meliata and Küre basins, Ladinian in the Maliac basin and Carnian in the Pindos basin; Stampfli et al., 2013). In the Pindos mountains of Greece, Upper Triassic *E*- and N-MORB-type lavas record the opening of the Pindos Ocean (Kostopoulos, 1989) to the west of Pelagonia (Fig. 1A).

The Pindos ophiolite, is Jurassic in age (ca. 171 Ma) based on SHRIMP U—Pb zircon crystallization ages of gabbros (Liati et al., 2004). It comprises two individual suites, one showing mid-ocean ridge, island-arc tholeiitic and boninitic affinities, the other being purely boninitic (Kostopoulos, 1989). These two suites have been interpreted as having been generated at a ridge-trench-transform intersection and a subduction forearc respectively (Kostopoulos, 1989). The Pindos ophiolite is separated from the Vourinos ophiolite to the east by the submarine siliciclastic deposits of the Mesohellenic Trough, a large, elongate (300x30x4.5 km) orogenic basin trending NW-SE, from northern Albania to central Greece, that operated from the Upper Eocene (ca. 45 Ma) to the Middle Miocene (ca. 15 Ma; Ferrière et al., 2013) (Fig. 1A). The two massifs are likely connected as part of a large mafic-ultramafic oceanic slab beneath the Mesohellenic Trough as evidenced by the presence of a massive positive magnetic anomaly corresponding to an ultramafic "keel" deep beneath the sedimentary strata (Rassios et al., 2009; Rassios and Dilek, 2009).

Metamorphic-sole rocks include metasediments and metabasites that occur as thin (less than 200 m), sheet-like bodies structurally below serpentinised mantle peridotite (Fig. 1B; after Rassios and Moores,

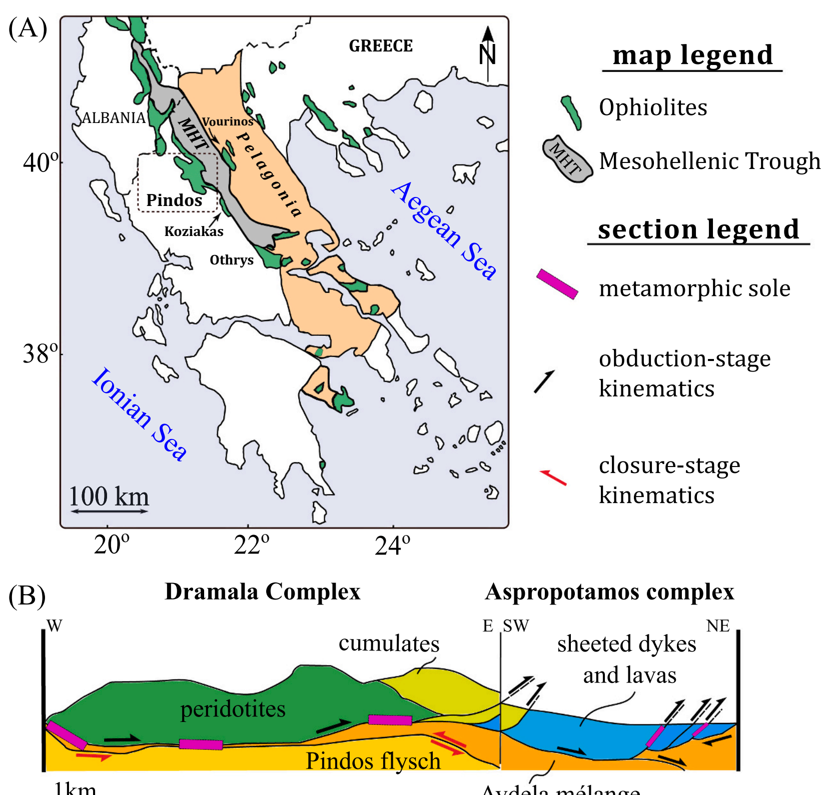

Fig. 1. Regional geology of the Pindos ophiolite. (A) Distribution of the main ophiolitic complexes in mainland Greece and Albania. Data compilation from Gartzos et al. (2009), Robertson et al. (1991), Smith et al. (1979), Smith (1993) and Smith and Spray (1984). The Pindos ophiolite is highlighted in the dashed quadrangle. (B) Simplified geological section for the Pindos ophiolite. The section has been simplified and modified after Rassios and Moores (2006) and Sergeev et al. (2014).

2006). According to Kemp and McCaig (1984) and Kostopoulos (1989 and references therein), the lower part of the sole comprises greenschist-facies metabasites, calcareous schists, graphitic schists, marbles, micaceous quartzites and garnet-mica schists while the upper part predominantly contains banded amphibole schists, epidote-amphibolite, and garnet amphibolite. These rocks are thought to represent a metamorphic aureole formed during the initial "displacement" of the ophiolite in the oceanic regime (Jones and Robertson, 1991; Spray, 1984). Hornblende separates from the amphibolites have yielded respective $^{40}Ar/^{39}Ar$ ages of 169 Ma (Spray et al., 1984).

3. Samples and Methods

The present study focuses on the metamorphic conditions of a metapelite sample from the metamorphic sole of the Pindos ophiolite (Liagouna locality: 39°59′18.6″, 21°11′14.8″ discussed in Kostopoulos, 1989). Additionally, an amphibolite sample was investigated from the same locality. Both metapelitic and amphibolitic samples were taken approximately 100 m away from the contact with the peridotites. Ten (10) thin sections from the same metapelitic sample and three (3) thin section from the amphibolite were thoroughly examined by means of transmitted-light microscopy (plane- and cross-polarized light), Electron Probe Micro Analysis (EPMA) and Scanning Electron Microscopy (SEM). All metapelitic thin sections showed identical features. Particular care was taken to collect orientated samples in the field and four of the studied thin sections were carefully cut parallel to the lineation and perpendicular to the foliation to provide details on the kinematics of ductile structures. S—C shear bands, fabric asymmetry and spiral inclusions in garnet were used as kinematic indicators. EPMA analyses were conducted at the Institute of Geosciences, Johannes Gutenberg University, Mainz, Germany. Further details on the equipment used and operating conditions can be found in Burg and Moulas (2022; their supplementary material). The amphibolite was measured at the Institute of Geosciences of the Goethe University of Frankfurt with a JEOL 8530F Plus Hyperprobe that comprises 5 wavelength-dispersive spectrometers. An accelerating voltage of 15.0 kV and a beam current of 20 nA were used. Synthetic and natural standards were utilized for the calibration of the machine. The beam diameter was set to either 1 or 2 μm. The peak measurement time was set to 20.0 s and the PRZ ARMSTRONG correction was applied.

$^{40}Ar/^{39}Ar$ geochronological analyses on mineral separates were carried out for the metapelite and amphibolite lithologies of the metamorphic sole. Specifically, a magnesio-hornblende separate from the amphibolite and a *syn*-kinematic muscovite from the metapelite were investigated. The measurements were carried out at Oregon State University using an incremental, bulk-laser heating technique. To derive representative mineral ages, we relied on consistent apparent age measurements observed across incremental heating steps. The released ^{39}Ar was monitored and we focused on data points where age values remained stable (age plateau) over increasing cumulative amounts of ^{39}Ar. A detailed description of the analytical procedure is provided in the supplementary material, and all measurement data are documented in the accompanying supplementary spreadsheet.

Uranium-lead (U—Pb) dating was conducted at the Frankfurt Isotope and Element Research Center (FIERCE) at the Goethe University of Frankfurt (Germany) using a Thermo-Scientific Neptune Plus Multi-Collector Laser Ablation Inductively–Coupled Plasma–Mass Spectrometer (MC LA-ICP-MS). In situ measurements were acquired using a RESOlution 193 nm ArF Excimer laser. More details on the analytical techniques and acquired measurements can be found in the supplementary material and provided spreadsheet.

To constrain the pressure and temperature (*P-T*) conditions of the metapelite, we performed phase-equilibria modelling using the PERPLE_X software package (Connolly, 2009). An effective bulk composition (EBC) for the metapelite was used in which only the outer 5 % of garnet was considered. Exact details on the determination of the EBC can be found in the supplementary material. The total bulk composition of the metapelite was also used for comparison (Table S1). We carried out two different series of calculations. In the first one, we have utilized the KNCFMASH (K_2O-Na_2O-CaO-FeO-MgO-Al_2O_3-SiO_2-H_2O) model system and the thermodynamic dataset of Holland and Powell (1998, with updates) as given in PERPLE_X. In this system, we have simplified the bulk composition by leaving out TiO_2 and MnO because of the limited number of experiments performed to calibrate the respective solid solution models. The second set of calculations was performed in the KNCFMASH + Mn (K_2O-Na_2O-CaO-FeO-MgO-Al_2O_3-SiO_2-H_2O-MnO) model system using the more recent thermodynamic database of Holland and Powell (2011) as in Green et al. (2016) (hp62ver). In this instance, MnO was included because the corresponding solid-solution models for garnet, biotite and chlorite were calibrated by considering Mn. Details on the solid solution models and the relevant H_2O equations of state used in each case can be found in the supplementary material.

In both cases, we have produced isochemical, pressure-temperature phase-diagram sections (*P-T* sections) either in water-saturated conditions or with a fixed amount of water. Moreover, isobaric temperature-composition (*T-X*) sections were modelled. These were supplemented by conventional geothermometry using adjacent garnet-biotite (Hodges and Spear, 1982; Kaneko and Miyano, 2004; Kleemann and Reinhardt, 1994), muscovite-paragonite compositional pairs (Blencoe et al., 1994; Coggon and Holland, 2002), adjacent garnet-muscovite pairs (Wu and Zhao, 2006) and garnet-phengite (Green and Hellman, 1982).

Finally, we applied elastic barometry where we used Raman spectroscopic analyses on quartz inclusions from metapelite garnets. The quartz spectra were obtained at the National Technical University of Athens (Greece), utilizing a Renishaw Ramascope RM1000 Raman spectrometer coupled with a Leica DM LM optical microscope. A natural, strain-free quartz crystal was employed as a reference standard to capture the reference 206 and 464 cm^{-1} peaks of quartz. A total number of 35 quartz inclusions in garnet were analyzed. We mostly focused on spherical quartz inclusions away from fractures or other inclusions to avoid geometric complexities and non-elastic contributions (for corresponding references see supplementary material). We additionally avoided cracks or features that could possibly relax stresses. The final spectra were fit with a Lorentzian curve using MATLAB® to accurately capture the shifted positions of the 206 and 464 cm^{-1} vibrational modes of quartz. Further methodological details and analytical parameters are provided in the supplementary material.

4. Results

4.1. Petrography

The metapelites (sample VK24) display a clear foliation defined by white mica (undifferentiated), quartz, and K-feldspar ribbons (Fig. 2A); minor biotite can also be found along the foliation planes. Garnet occurs as porphyroblasts (half a mm in diameter) in the matrix (Fig. 2). Small bands composed entirely of quartz and minute garnets (<0.1 mm in diameter) occur locally (Fig. 2B). At the rims of these small bands, the two garnet sizes can be seen together along with rutile and tourmaline (Fig. 2C). K-feldspar is observed both in the matrix and at the rims of the quartz-rich bands (Fig. 3). In many cases, K-feldspar is observed crystallizing at the rims of garnet (Fig. 4) or within cracks cutting garnet (Fig. 3D, Fig. 5). The K-feldspar forming inside these cracks is often found together with quartz (K and Si map in Fig. 5). White mica is composed of muscovite-rich and paragonite-rich laths which become visible in a K map (Figs. 4, 6). In one case, K-feldspar was found developing at the rim of a large, white mica lath (Fig. 3D). Other phases found in smaller amounts in the matrix are plagioclase (albite-rich) and chlorite. The plagioclase is often concentrated in small domains together with quartz and K-feldspar (Fig. 6) whereas chlorite replaces biotite at the rims of garnet (Fig. 4). Titanium-bearing accessory phases are also

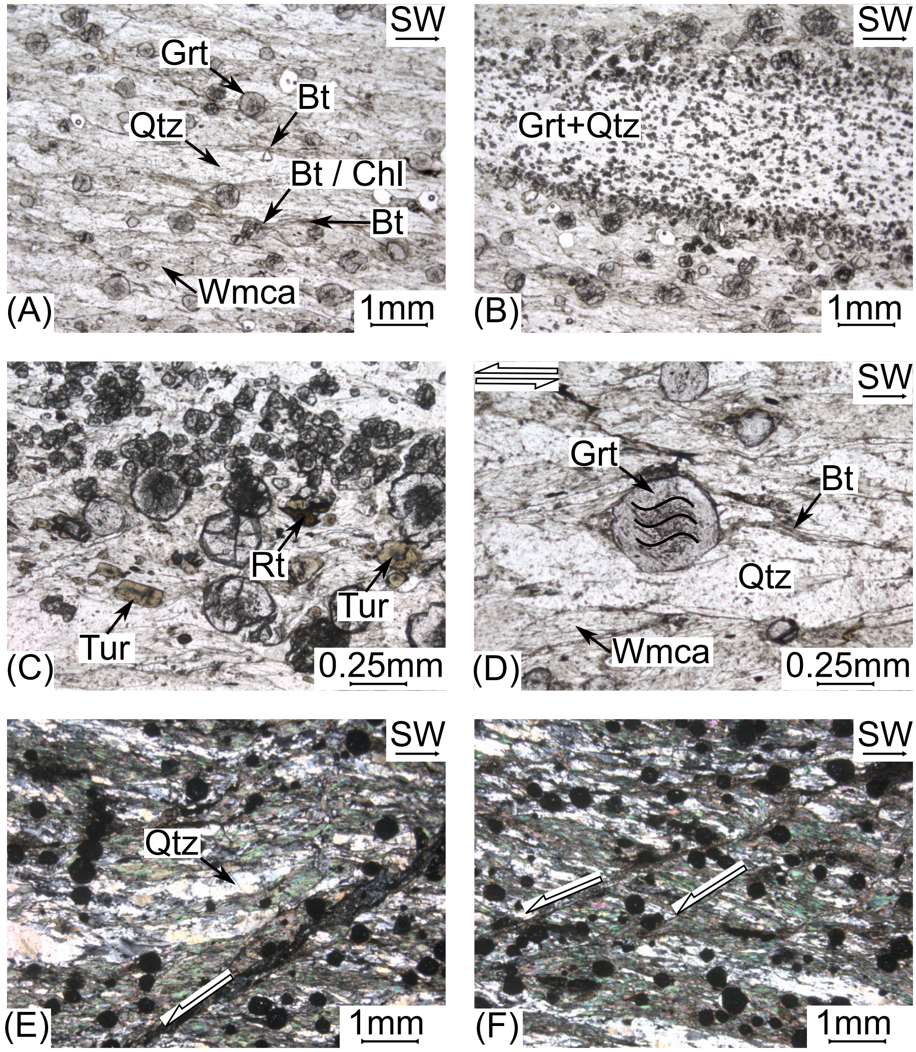

Fig. 2. Photomicrographs of the garnet-mica schist from the Pindos sole displaying the most important textures observed. Mineral abbreviations after Siivola and Schmid (2007). (A) White mica (undifferentiated) and garnet porphyroblasts in the rock's matrix. (B) Millimetric band composed entirely of minute garnet and quartz. (C) Detail from (B) focusing on the contact between the thin quartz-garnet band and the matrix. (D) Syn-kinematic garnet porphyroblast showing apparent top-to-the-NE rotation. (E) Asymmetric quartz ribbons and S—C shear bands indicating top-to-the-NE shearing (crossed polars). (F) S—C shear bands indicating top-to-the-NE shearing (crossed polars).

present. Manganoan-ilmenite occurs as inclusions in garnet while rutile is widespread in the matrix (Fig. 2C).

Kinematic indicators from quartz inclusion trails indicate the *syn*-kinematic growth of garnet (Fig. 2D). In the majority of garnet porphyroblasts, the spiral-shape of quartz inclusions indicate a top-to-the NE shear of the garnet with respect to its surrounding matrix. However, some garnet porphyroblasts have been observed to have the opposite sense of shear. Nevertheless, in all of the investigated oriented thin sections, the asymmetric quartz ribbons and S—C bands in mica undoubtedly indicate a top-to-the-NE sense of shear (Fig. 2E-F).

The amphibolite (sample VK25) is equigranular in texture and exhibits a distinct foliation defined by green amphibole. The amphibole appears primarily as idiomorphic crystals ranging from 0.3 to 0.8 mm in diameter, though occasional larger crystals exceeding 2 mm are also present (Fig. S1A, B). Amphibole constitutes a dominant 65–70 vol% of the rock. Titanite was found as an inclusion in amphibole. The remaining matrix is comprised of a very fine-grained intergrowth. The intergrowth has fully replaced plagioclase and is mostly comprised of fine-grained muscovite (sericite) and possibly epidote or prehnite (Fig. S1C, D; supplementary material).

4.2. Mineral and bulk rock chemistry

The studied metapelitic sample shows a sedimentary affinity based on a Zr/Ti vs Ni classification and plots at the low-Al field of common metapelites in an AFM diagram (projected from muscovite and corrected for paragonite) (Fig. S2; supplementary material). Representative mineral analyses are given in Table 1. In general, most minerals show a uniform composition except for garnet porphyroblasts that show a prominent zonation in Ca (Figs. 4–6). Matrix garnet falls in the range: $Prp_{13\text{-}22}Alm_{72\text{-}78}Grs_{0.02–0.08}Sps_{0.02–0.06}$. Their grossular and spessartine components decrease and X_{Mg} (i.e., $Mg/[Mg+Fe]$; molar ratios) increases from core to rim. A representative X_{Mg} value at the garnet rim is 0.2 ± 0.02. The smaller garnets of the quartz-rich band (e.g., Fig. 2B) are richer in MnO and characterized by the composition: $Prp_{16\text{-}17}Alm_{57\text{-}58}Grs_{0.11–0.13}Sps_{0.14}$. The few ilmenite inclusions in garnet are manganoan containing ca. 27 % pyrophanitic component $(Fe_{0.73}Mn_{0.27})TiO_3$.

Biotite shows a uniform composition with X_{Mg} stretching between 0.57 and 0.60. Chlorite replacing biotite shows X_{Mg} values from 0.47 to 0.53 with an average of 0.51. White mica has a variable X_{Mg} content depending on whether it is muscovite- or paragonite-rich. Muscovite-

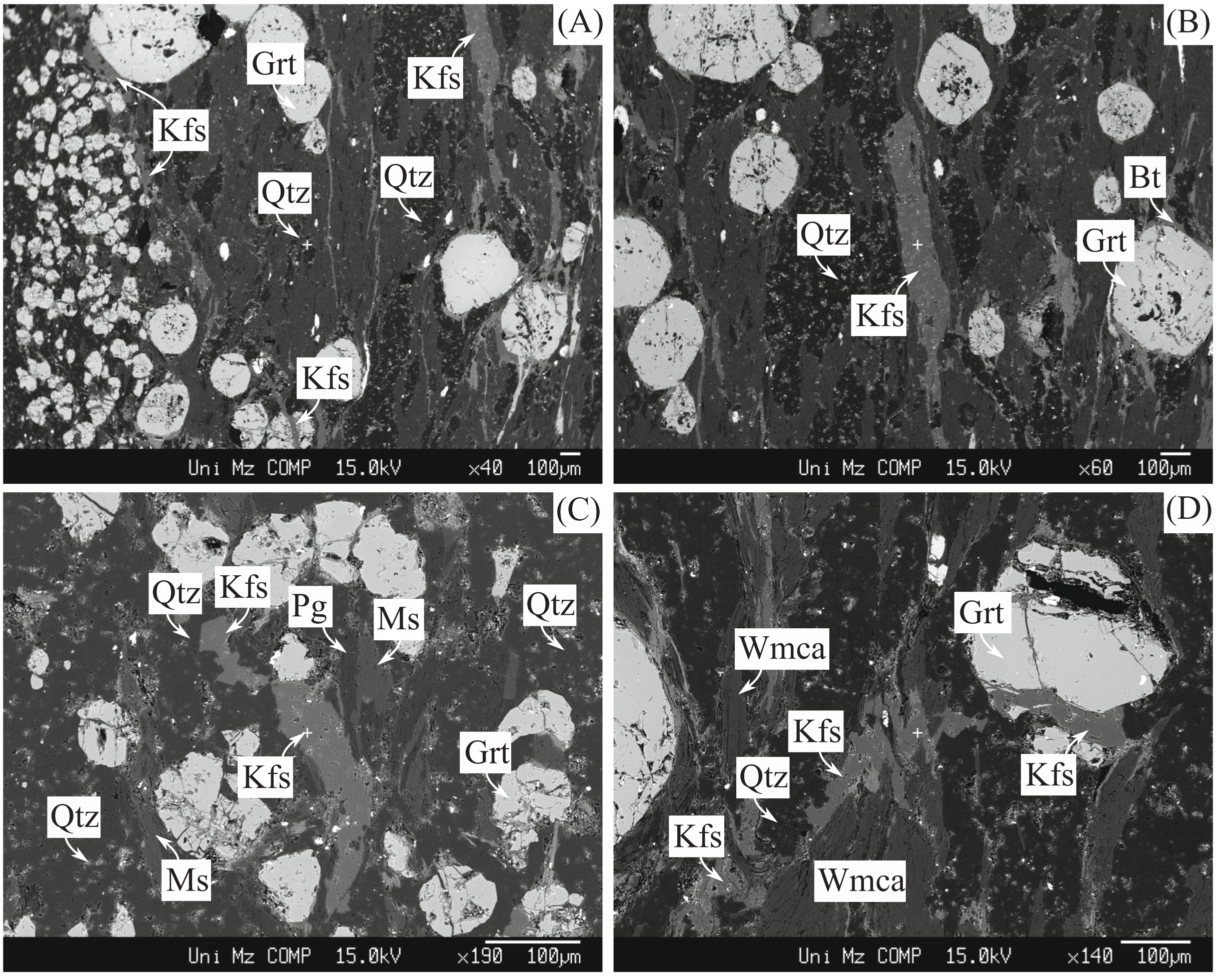

Fig. 3. Back-Scattered Electron images of the main textures observed. (A) The contact between the rock matrix (left) and the thin, quartz-rich band (right). (B) K-feldspar observed in a region rich in quartz and garnet. (C) Garnet porphyroclasts in a matrix of white mica (muscovite and paragonite) and quartz. Note the large K-feldspar lath in the center of the image. (D) K-feldspar occurring both at the rims of a white mica lath (undifferentiated) and in garnet cracks.

rich white mica has an average X_{Mg} of 0.61 whereas paragonite-rich white mica has an X_{Mg} between 0.25 and 0.56 with an average of 0.41. The plagioclase found in association with K-feldspar and quartz (Fig. 6) is sodic with X_{Ab} (i.e., $Na/[Na+Ca]$; molar) ranging from 0.82 to 0.94. K-feldspar maintains the same composition across all textures, with a $K/[K+Na+Ca]$ molar ratio ranging from 0.97 to 0.99.

The representative chemical composition of amphibole from the amphibolite is also shown in Table 1. We used the Excel spreadsheet of Locock (2014), which follows the latest nomenclature for the amphibole supergroup (Hawthorne et al., 2012), to calculate the chemical formula of amphibole. Assuming total iron is ferrous, the amphibole can be classified as a magnesio-hornblende. Including ferric iron, the nomenclature predicts a $Fe^{+3}/\Sigma Fe$ ratio of ~0.088 and the classification of the amphibole is not affected. The composition of amphibole is uniform from grain to grain but also from core to rim. The ranges of Mg, Fe and Ca are 3.32–3.56, 0.58–0.72 and 1.91–1.98 a.p.f.u., respectively. The intergrowth that replaces plagioclase comprises two mineral phases. The most abundant phase (~85 vol%) is a fine-grained muscovite (sericite) which has a K/(K + Na) ratio of 0.98. The remaining intergrowth consists of a fine-grained hydrous phase primarily composed of Si, Ca, and Al. This phase was highly susceptible to beam damage which prevented accurate measurements and resulted in unsatisfactory oxide totals. However, this phase could be identified as either epidote or prehnite.

4.3. Ar—Ar geochronology

The results of the $^{40}Ar/^{39}Ar$ geochronology are presented in Fig. 7. Apparent ages are plotted against the cumulative ^{39}Ar released per heating step (age spectrum plot). Final ages were determined by identifying age plateaus. For the amphibole, several initial measurements showed large 2σ errors. However, a distinct and well-defined age plateau yields a Jurassic age of 165.5 ± 0.73 Ma (2σ). The preservation of the age-plateau indicates that there was no loss of Ar and that amphibole was unaffected by diffusion or secondary processes. Conversely, the *syn*-kinematic muscovite is defined by insignificant analytical errors. However, initial heating steps have shown notable amounts of Ar loss. Progressive incremental heating led to a rapid increase of the apparent age as shown from the age plateau defined by the last heating steps. This pattern could be related to volume diffusion of Ar (e.g., Wijbrans and McDougall, 1988) or alteration processes. During the final incremental heating steps (from ~78 % of ^{39}Ar released), a minimum age plateau was observed, defining an age of 164.16 ± 0.37 Ma (2σ). Notably, the radiogenic Ar compositions at the rim of muscovite during the initial steps yielded a Cretaceous age of approximately 78 Ma (Fig. 7B).

4.4. U—Pb geochronology

The results of U—Pb geochronology of garnets from the metapelite of the Pindos metamorphic sole are presented in a Tera-Wasserburg plot as

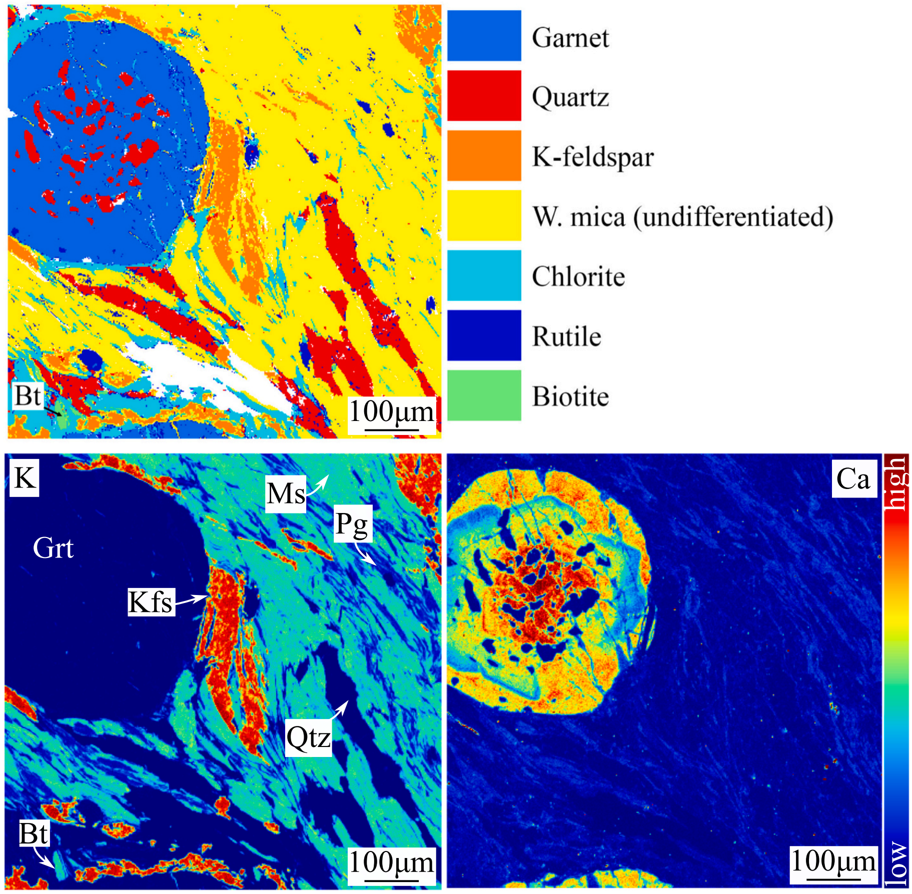

Fig. 4. (Top) Mineral map constructed using individual elemental distributions. (Bottom) K and Ca distribution maps.

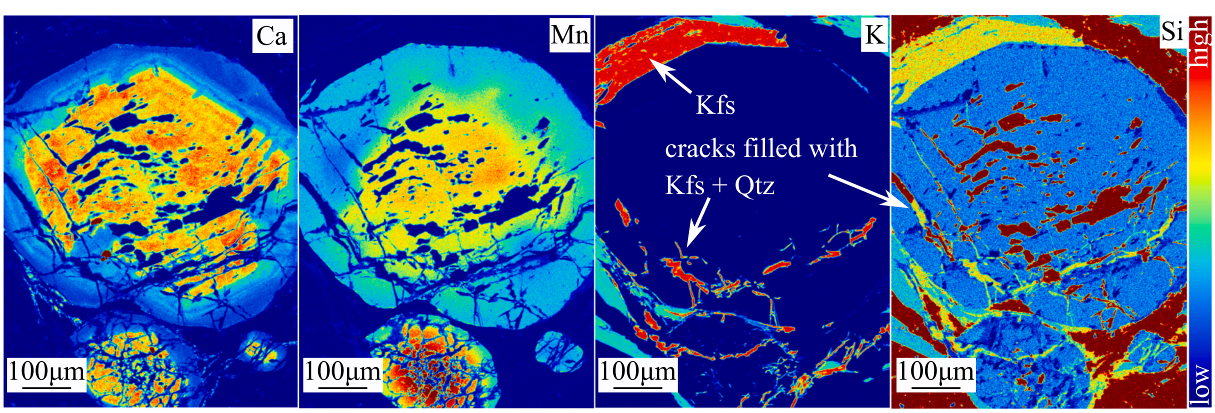

Fig. 5. Ca, Mn, K, and Si distribution maps of a large garnet porphyroblast. Note the cracks filled with K-feldspar and quartz.

seen in Fig. 8. The analytical results are also given in detail in the supplementary material. Generally, U, Th, and Pb content show a large variability, with concentrations up to 10 μg/g of U or 159 μg/g of Th. The amount of radiogenic and common Pb is also variable. This variability allows the determination of a regression line that intersects the concordia curve at 178.5 ± 4.8 Ma (2σ). However, upon careful examination of the time-resolved analyses, it is most likely that the elevated concentrations of U and Th are attributable to the presence of inclusions, specifically zircon and/or rutile in the case of high U and monazite in the case of high Th contents.

4.5. Phase-equilibria and thermobarometric estimations

The estimation of the peak metamorphic conditions attained by the metapelite was based on i) petrographical evidence, ii) phase-equilibria modelling and iii) mineral thermobarometry. The assemblage garnet-biotite-muscovite-paragonite-plagioclase-quartz (GBMPPQ) in metapelites is indicative of high-grade ($T > 600\,^{\circ}$C and P ~ 1GPa) conditions (Tinkham et al., 2001, p. 12). Chlorite is observed to replace biotite and therefore is not considered as part of the peak-*T* assemblage. The GBMPPQ assemblage, however, does not explain the presence of large crystals of syn-kinematic K-feldspar in the rock (Fig. 4). To investigate the stability of K-feldspar, we used isochemical phase diagrams under two different sets of conditions and using two different thermodynamic

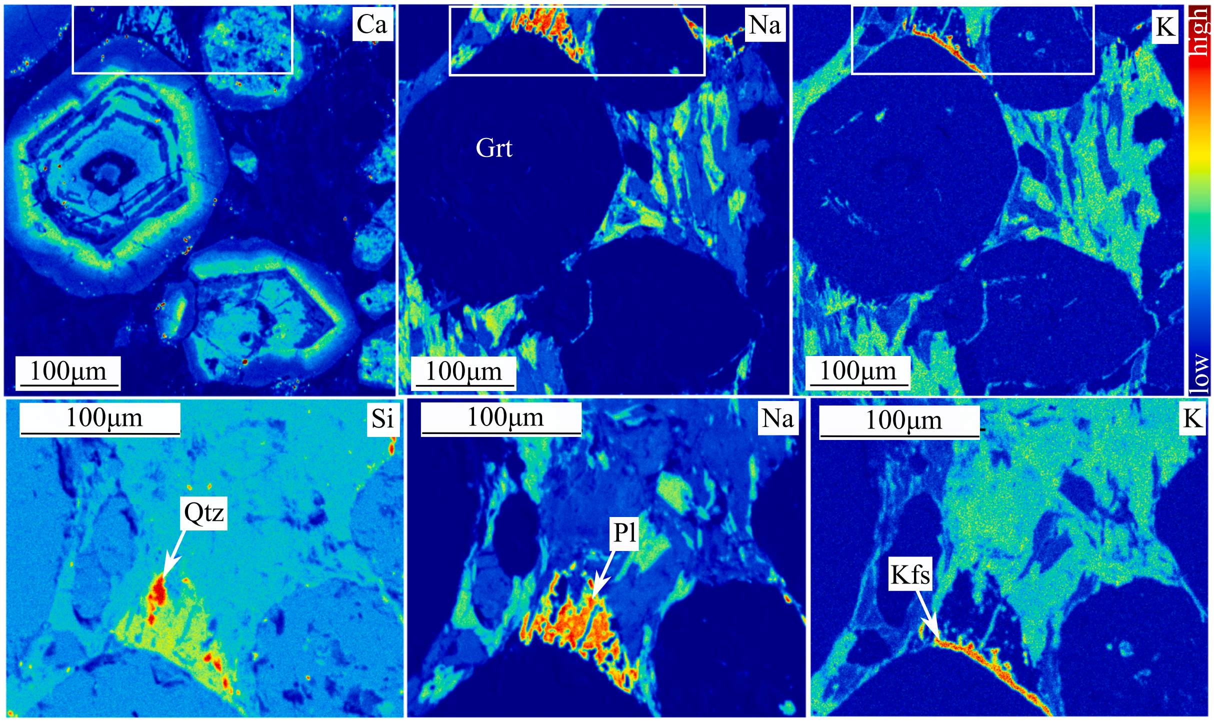

Fig. 6. Ca, Na, K (top row) and Si, Na, K (bottom row) maps from a region rich in garnet porphyroblasts. The white rectangle marks the area with quartz-plagioclase-K-feldspar intergrowths (details in bottom row).

datasets (Holland and Powell, 1998; Holland and Powell, 2011). With both datasets we first examined water-saturated conditions. Subsequently, to simulate water-undersaturated conditions, we introduced a fixed amount of water (3.17 wt%) in order to stabilize hydrous minerals while maintaining a controlled level of water undersaturation. The Effective Bulk Composition (EBC) was determined using mineral modal abundances of the rock matrix as depicted in Fig. 4 and their compositions. For garnet, only the outer (last 5 % of garnet radius) rim composition was used whereas its core composition was not considered in the determination of the EBC (see supplementary material for details).

Regardless of the water-content and across both datasets, we found no stability field in which K-feldspar coexisted with the GBMPPQ assemblage (Fig. 9 and Fig. S3 of the supplementary material). Notably, in water-saturated conditions the coexistence of any kind of feldspar along with muscovite and paragonite is unfavorable (Fig. 9A and Fig. S3A of the supplementary material). Meanwhile, under water-undersaturated conditions, albite or albite-rich plagioclase became stable (Fig. 9B and Fig. S3B of the supplementary material). Considering this observation, we further explored the role of H_2O in the stability of feldspar. Therefore, we constructed *T-X* sections at constant pressure (1.1GPa). In these sections, H_2O (*X*) varies from 2.19 to 4.13 (wt%). Fig. 9C and Fig. S3C illustrate that K-feldspar can become stable within a narrow range of water content, from 2.19 to 2.4 wt%. However, kyanite and a single white mica phase are also stable in this field alongside K-feldspar. This assemblage does not correspond to the one observed in the studied rock. K-feldspar can also be present along with kyanite at temperatures exceeding 775 °C. Evidently, the equilibrium approach followed here is not enough to explain the presence of K-feldspar. Therefore, different scenarios for the formation of K-feldspar have been considered (see discussion).

The isochemical *P-T* sections were also used to delineate the range of the *P-T* conditions of equilibrium that are indicated by the mineral chemistry of the coexisting phases. In the case of H_2O-saturated conditions and the dataset of Holland and Powell (1998) (Fig. 9A), the observed GBMPPQ assemblage and the compositions of the coexisting minerals indicate 636 ± 10 °C and 1.07 ± 0.1 GPa as average *P-T* conditions (see Fig. S4 of the supplementary material for the compositional isopleths). At these conditions, a small volume fraction of melt (<8 %) is predicted. For H_2O-saturated conditions we additionally tested the total bulk composition and we obtained similar conditions but not a satisfactory fit of compositional isopleths (Fig. S5 of the supplementary material). For the case of H_2O-undersaturated conditions (H_2O: 3.17 wt%), the observed GBMPPQ assemblage and the compositions of coexisting biotite, garnet and muscovite point to 634 °C ± 18 °C and 1.09 ± 0.07 GPa (Fig. 9B). These results are in accordance with the water-saturated case. The predicted amount of melt in this case is less than 2 % (by volume; Fig. S4B). Finally, the results for the *T-X* section show the best fit (both in mineral assemblages and mineral compositions) at about X:0.60 ± 0.09 (i.e., H_2O: 3.35 wt%), T:631 ± 13 °C and at 1.1 GPa (Fig. S3 of the supplementary material for details).

The results using the thermodynamic dataset Holland and Powell (2011) show a ~ 45 °C shift of the solidus toward higher temperatures (Fig. S3 of the supplementary material). Additionally, biotite is no more stable beyond the solidus. Therefore, the calculated average *P-T* conditions can only lie below the solidus. The compositional isopleths representing the observed compositions of garnet, biotite, and muscovite do not cross-cut each other as closely as they do with the dataset of Holland and Powell (1998) (Fig. S6 of the supplementary material). Although the fit is not optimal, the derived average *P-T* conditions are very similar. For water-saturated conditions the best fit is obtained at 621 °C ± 15 °C and 1.25 ± 0.05 GPa (Fig. S6 of the supplementary material). For a fixed amount of water (H_2O: 3.17 wt%) the best-fit temperature is 621 °C ± 15 °C and the best-fit pressure is 1.19 ± 0.05 GPa. In the *T-X* section, we calculated a temperature of 617 °C ± 15 °C and approximately 3.37 wt % H_2O at a constant pressure of 1.1 GPa.

The error (2 σ) ellipse in all cases was calculated using the compositions of the coexisting garnet, white mica (muscovite-rich) and biotite. We used the average X_{Mg} rim values of coexisting minerals and calculated a misfit (or error) function of the form:

$$\Omega = \left(X_{Mg}^{Grt} - Y_{Mg}^{Grt}\right)^2 + \left(X_{Mg}^{Bt} - Y_{Mg}^{Bt}\right)^2 + \left(X_{Mg}^{WMca} - Y_{Mg}^{WMca}\right)^2$$

Table 1
Representative mineral compositions (wt%). Amph12 is a representative magnesio-hornblende from the amphibolite. Mineral abbreviations after Siivola and Schmid (2007). Norm [O] indicates the number of oxygen atoms used in the recalculation of the atoms per formula unit (a.p.f.u.).

Comment	E12	L2_91	E1	E3	E7	E8	E10	L19_134	L59_174	Can17	Can16	S4_D02	An8	S3_D15	Amph12	Ser1
Abbr.	**Kfs**	**Kfs**	**Pl**	**Pl**	**Wmca**	**Wmca**	**Grt**	**Grt**	**Grt**	**Grt**	**Bt**	**Bt**	**Chl**	**Chl**	**Hbl**	**Ser**
SiO_2	62.53	64.82	65.92	64.41	46.41	46.36	38.21	37.96	38.14	38.52	36.60	36.00	29.12	29.82	47.24	45.98
TiO_2	0.02	0.01	0.04	0.02	0.27	0.53	0.17	0.12	0.02	0.03	1.32	0.84	0.10	0.07	0.23	0.01
Al_2O_3	17.94	18.25	20.49	21.67	38.05	35.48	21.09	21.40	22.04	21.42	18.86	20.00	18.93	18.00	12.19	36.01
FeO	2.28	0.55	0.52	0.36	0.74	0.95	30.67	31.10	33.81	33.51	16.85	15.95	24.61	23.65	5.43	0.19
MgO	1.31	0.03	0.08	0.02	0.37	0.81	4.04	2.49	4.28	4.93	12.88	13.35	14.39	16.19	16.62	0.65
MnO	0.09	0.05	0.06	0.05	0.04	0.03	3.58	5.65	0.97	0.65	0.14	0.08	0.51	0.52	0.08	0.00
CaO	0.03	0.00	1.18	2.66	0.26	0.06	3.41	3.18	2.22	2.51	0.16	0.02	0.16	0.19	12.67	0.27
Na_2O	0.16	0.17	10.98	10.33	5.59	2.51	0.00	0.01	0.10	0.00	0.37	0.38	0.05	0.01	1.59	0.17
K_2O	14.89	16.11	0.70	0.20	2.55	7.29	0.00	0.00	0.02	0.01	7.19	7.97	0.30	0.15	0.06	11.15
Cr_2O_3	0.02	0.00	0.03	0.00	0.06	0.03	0.05	0.06	0.04	0.04	0.07	0.00	0.00	0.09	0.12	0.00
Total	99.27	99.99	100.00	99.73	94.35	94.04	101.23	101.96	101.64	101.62	94.45	94.60	88.18	88.68	96.23	94.43
Norm [O]	**8.00**	**8.00**	**8.00**	**8.00**	**11.00**	**11.00**	**12.00**	**12.00**	**12.00**	**12.00**	**11.00**	**11.00**	**14.00**	**14.00**	**24***	**11.00**
a.p.f.u.																
Si	2.93	3.00	2.91	2.85	3.02	3.08	3.01	3.00	2.99	3.01	2.74	2.69	3.03	3.06	6.74	3.07
Ti	0.00	0.00	0.00	0.00	0.01	0.03	0.01	0.01	0.00	0.00	0.07	0.05	0.01	0.01	0.02	0.00
Al	0.99	1.00	1.07	1.13	2.92	2.78	1.96	1.99	2.03	1.97	1.66	1.76	2.32	2.18	2.05	2.84
Fe	0.09	0.02	0.02	0.01	0.04	0.05	2.02	2.05	2.21	2.19	1.05	1.00	2.14	2.03	0.65	0.01
Mg	0.09	0.00	0.01	0.00	0.04	0.08	0.47	0.29	0.50	0.57	1.44	1.49	2.23	2.48	3.54	0.06
Mn	0.00	0.00	0.00	0.00	0.00	0.00	0.24	0.38	0.06	0.04	0.01	0.01	0.05	0.04	0.01	0.00
Ca	0.00	0.00	0.06	0.13	0.02	0.00	0.29	0.27	0.19	0.21	0.01	0.00	0.02	0.02	1.94	0.02
Na	0.01	0.02	0.94	0.89	0.71	0.32	0.00	0.00	0.01	0.00	0.05	0.05	0.01	0.00	0.41	0.02
K	0.89	0.95	0.04	0.01	0.21	0.62	0.00	0.00	0.00	0.00	0.69	0.76	0.04	0.02	0.01	0.95
Cr	0.00	0.00	0.00	0.00	0.00	0.00	0.00	0.00	0.00	0.00	0.00	0.00	0.00	0.01	0.01	0.00
Total	**5.02**	**4.99**	**5.04**	**5.03**	**6.97**	**6.97**	**8.00**	**8.00**	**8.00**	**8.00**	**7.73**	**7.79**	**9.83**	**9.85**	**15.38**	**6.97**
Ca/(Ca + Na)			0.06	0.12												
K/(K + Na)					0.23	0.66										0.98
Mg/(Mg + Fe)							0.19	0.12	0.18	0.21	0.58	0.60	0.51	0.55		

*24(O, OH, F, Cl) with (OH, F, Cl) = 2 a.p.f.u. after Hawthorne et al. (2012).

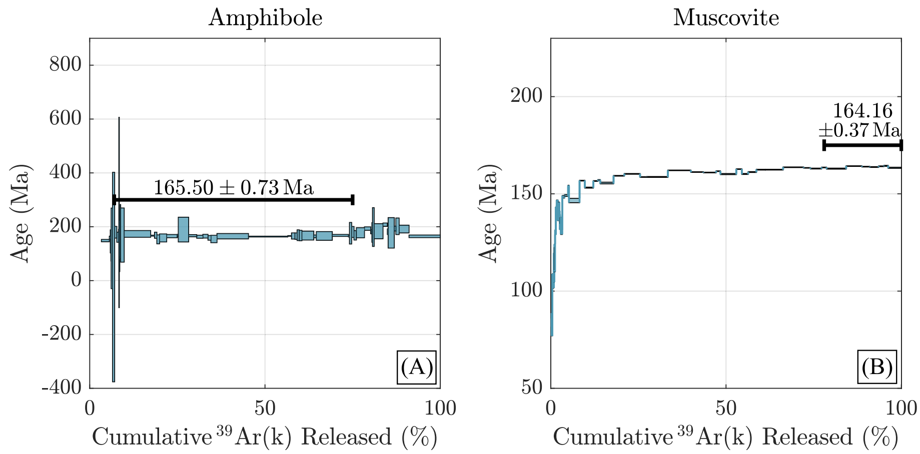

Fig. 7. Ar—Ar age spectrum plots for amphibole (A) and *syn*-kinematic muscovite (B) separates from the Pindos ophiolitic sole. Amphibole shows a well-defined age plateau at 165.5 ± 0.73 Ma (2σ). Muscovite exhibits Ar loss but shows an age plateau of 164.16 ± 0.16 Ma (2σ). See main text for more details.

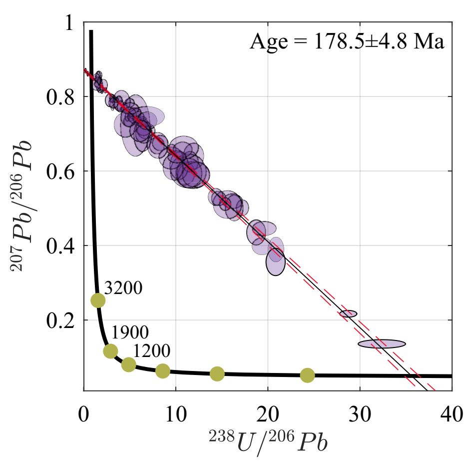

Fig. 8. Tera-Wasserburg plot illustrating the U—Pb isochron for garnets from the studied metapelite. The regression yielded an age of 178.5 ± 4.8 Ma.

where Ω is the misfit, X_{Mg} is the measured value of $Mg/(Mg+Fe)$ in the respective mineral, and Y_{Mg} is the modelled value as it is given by the routine "werami" in PERPLE_X. A good fit in the mineral compositions is where Ω is minimized in *P–T* space (i.e., when observed and modelled mineral compositions coincide; see also Hunziker et al., 2017 and Nerone et al., 2025). For the case of crossing isopleths, this approach is equivalent to finding the points of intersection of three respective compositional isopleths $\left(X_{Mg}^{Grt}, X_{Mg}^{Bt}, X_{Mg}^{WMca}\right)$. At the intersection points, $\Omega = 0$. The exact intersection points can be observed in Fig. S4, Fig. S5 and Fig. S6 of the supplementary material.

To gain insight on the relative error of the estimated *P–T* conditions we performed a Monte Carlo analysis by perturbing the mean X_{Mg} by 1 % in a random manner following a normal distribution of errors (as in Moulas et al., 2020). The perturbation of the respective X_{Mg} values was repeated 2000 times. This perturbation agrees very well with the measured X_{Mg} ranges in all three minerals. Thus, for each combination of randomly perturbed $X_{Mg}^{Grt}, X_{Mg}^{Bt}$ and X_{Mg}^{WMca} values, the minimum point of the misfit function (Ω) was found in *P–T* space. The optimal conditions were derived by taking the average values of the best-fit points and using them to calculate their mean values and covariance.

To constrain the *P-T* conditions even further, we performed conventional thermobarometry. Fig. 10 shows the results of garnet-biotite thermometry applied to porphyroblastic garnet rims and adjacent matrix biotite crystals. Assuming a pressure of about 1.1 GPa (see ensuing paragraph), the temperatures obtained are 619 ± 9 °C (1 σ), 632 ± 8 °C (1 σ) and 646 ± 16 °C (1 σ) for the calibrations of Kleemann and Reinhardt (1994), Kaneko and Miyano (2004) and Hodges and Spear (1982) respectively. Using additional calibrations did not alter the results, therefore we will not consider other formulations any further.

Numerical mica-solvus thermometry (Blencoe et al., 1994; their eq. 11) for twelve coexisting muscovite-paragonite pairs (Fig. 4; K map) yielded a temperature of 654 ± 33 °C (1 σ) (Fig. 11). The muscovite grains of these pairs are characterized by $Si_{a.p.f.u.}$ and X_{Ms} values of 3.09 ± 0.03 and 0.7 ± 0.03 respectively and give a temperature of 640 ± 15 °C when plotted on the muscovite limb of the two-mica solvus calculated for $Si_{a.p.f.u.} = 3.1$ at 1 GPa using the Coggon and Holland (2002) thermodynamic approach.

We additionally used the empirical garnet-muscovite, Fe—Mg exchange thermometer of Wu and Zhao (2006) and the garnet-phengite, Fe—Mg exchange thermometer of Green and Hellman (1982) (Fig. S7). The garnet-muscovite thermometer is an empirical formulation based entirely on natural data (Wu and Zhao, 2006). However, the *P-T* range of its applicability falls within our previously mentioned estimations. For a fixed pressure of 1.1 GPa and assuming all iron in muscovite is ferrous, we obtained an average temperature of 602 ± 7.8 °C (1σ). The garnet-phengite thermometer has been originally calibrated based on phengite-rich mica and also at high temperatures (>800 °C) and pressures (>20 kbar). By extrapolation we obtained a temperature of 674 ± 27 °C (1σ) at 1.1 GPa. Although the use of this thermometer under these conditions and bulk rock composition should be inappropriate due to its calibration range, it nonetheless provides temperature estimates that align well with previous calculations. This suggests that, despite the limitations of extrapolation, the results remain consistent within the context of this study.

The results from all thermobarometric methods employed consistently indicate that the peak conditions are in the order of 630 ± 20 °C at 1.1 ± 0.2GPa. These conditions are in accord with the onset of wet melting of relevant lithologies, constrained experimentally to lie at about ~630 °C at such pressures (see review by Weinberg and Hasalová, 2015). Thus, all pieces of thermobarometric and textural evidence suggest that the temperature was of the order of 630 °C.

4.6. Quartz in garnet elastic barometry

Apart from the classical thermobarometric methods discussed above, we also performed Quartz-in-Garnet (QuiG) elastic barometry. This method is based on the preserved residual pressures of quartz inclusions in garnet and can be used to obtain the apparent entrapment conditions. To calculate the residual pressure of quartz enclosed by garnet in our

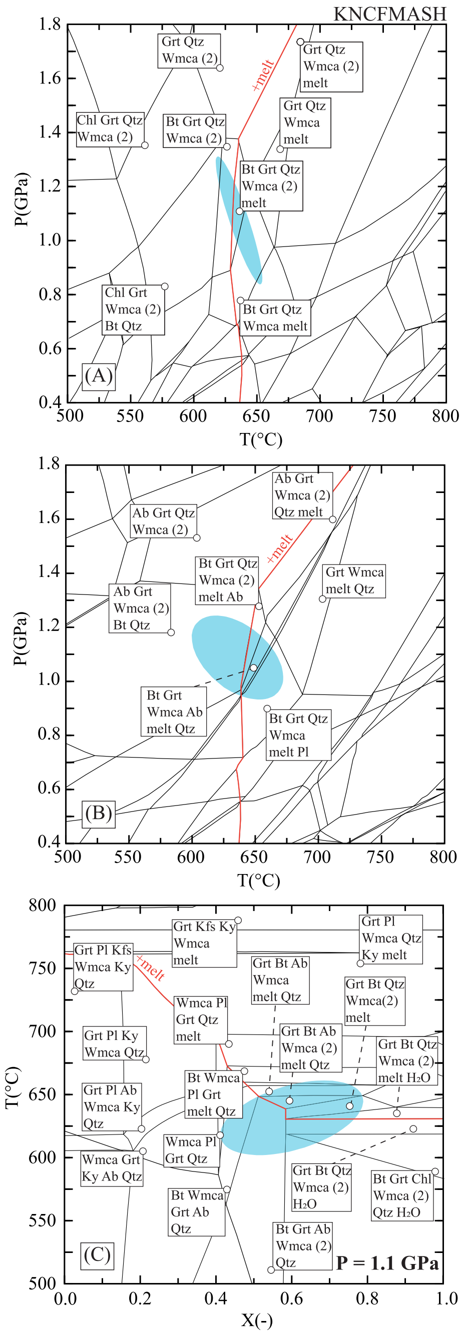

Fig. 9. Phase-diagram *P-T* and *X-T* sections of the investigated metapelitic sample. Red line is the solidus. The blue ellipse (2 σ) delineates the area in which the observed mineral compositions are best reproduced and were constructed with a Monte Carlo approach. (A) H_2O-saturated *P-T* section, (B) H_2O-undersaturated *P-T* section, (C) Variable H_2O, *X-T* section (at P:1.1GPa). The bulk compositions used to produce these diagrams are given in the supplementary material. Mineral abbreviations follow Siivola and Schmid (2007). (For interpretation of the references to colour in this figure legend, the reader is referred to the web version of this article.)

sample, we followed the method of Angel et al. (2019), also described in detail by Moulas et al. (2020). Briefly, this method utilizes the phonon-mode Grüneisen tensor in combination with the measured shifts of quartz vibrational modes to determine the strain components:

$$-\frac{\Delta\omega^m}{\omega_0^m} = \gamma_1^m(\varepsilon_1+\varepsilon_2)+\gamma_3^m\varepsilon_3$$

where $\Delta\omega^m$ is the wavenumber difference of the vibration mode m of quartz, ω_0^m is the reference quartz wavenumber of vibrational mode m, γ_i^m are the components i of the Grüneisen tensor and ε_i are the components of the strain tensor (in Voigt notation). The value of $\Delta\omega^m$ can be calculated by subtracting the measured Raman shifts of the 206 and 464 cm^{-1} vibrational modes of quartz from the reference values. The determination of the elastic strain components enables the calculation of the stress components with the use of the elasticity (stiffness) matrix of quartz (Appendix B in Moulas et al., 2020). Subsequently, pressure can be calculated as $P = -\frac{1}{3}(\sigma_1+\sigma_2+\sigma_3)$.

To avoid relaxed quartz inclusions, the maximum residual pressure of quartz in garnet was subsequently used to construct an isomeke. An isomeke represents a line in *P-T* space along which quartz and garnet coexist without developing a pressure difference (Angel et al., 2015). The choice of the maximum residual pressure for the construction of the isomeke aims to avoid inclusions that experienced relaxation due to fracturing or near-surface effects (Enami et al., 2007). We followed two different approaches to calculate the isomeke. In the first approach, we assume linear elasticity, constant thermoelastic properties and isotropy in the host-inclusion system as in Moulas et al. (2020). In the second approach, we utilized a non-linear solution of the inclusion-in-host problem that assumes the finite strain effects of the volumetric deformation but approximates the shear deformation using a small-strain assumption (Moulas et al., 2023). In this non-linear method, entrapment conditions can be determined once the volumes of quartz and garnet at initial and final *P-T* conditions are known. Therefore, relevant Equations of State (EoS) are required. An analytical description of the entire procedure, the Equations of State used as well as the parameters and moduli utilized for the elastic barometry in this paper are provided in the supplementary material.

The data presented in Fig. 12A highlight the existence of numerous quartz inclusions retaining residual pressures above 0.2 GPa. The highest calculated pressure was 0.387 GPa. This maximum pressure value was subsequently used to construct the isomeke plots of Fig. 12B. For an assumed temperature of 500 °C, the linear isomeke predicts an entrapment pressure of 1.08 ± 0.01 GPa (1σ). Using a temperature of 630 °C—in line with thermobarometric estimations—the mean entrapment pressure increases to 1.20 ± 0.01 GPa (1σ). For the case of the non-linear isomeke the results are comparable. A pressure of 1.12 ± 0.02 GPa (1σ) for 500 °C and 1.29 ± 0.02 GPa (1σ) for 630 °C were calculated. Considering the potential sources of error among the different methods employed, the QuiG barometry results are in agreement with our previously derived *P-T* conditions.

5. Discussion

5.1. Determination of peak metamorphic conditions

The evident consistency between petrographic observations and thermobarometric and phase equilibria calculations strongly suggests that the studied metapelitic sample from the Pindos metamorphic sole underwent upper amphibolite-facies conditions. The estimated temperature is 630 ± 20 °C while the estimated pressure is 1.1 ± 0.2GPa. These findings contrast with earlier studies (Jones et al., 1992 and references therein) that proposed greenschist-facies conditions for metapelites in the region. However, our results align closely with those reported for amphibolite-facies mafic lithologies in the Pindos sole (Jones and Robertson, 1991; Kemp and McCaig, 1984; Myhill, 2011). They also agree with similar lithologies in Albanian ophiolites (Dimo-Lahitte et al., 2001) and the Koziakas ophiolite to the south (Pomonis et al., 2002). Worth-mentioning here is the *P–T* determination of Myhill (2011, p. 87) for a garnet-bearing pyroxenite boudin present within a quartzofeldspathic shear-zone melt within mafic amphibolite from the very same locality in the Pindos sole. This anhydrous assemblage yields an optimal *P–T* estimate of 650 °C and 1 ± 0.1GPa for a water activity of

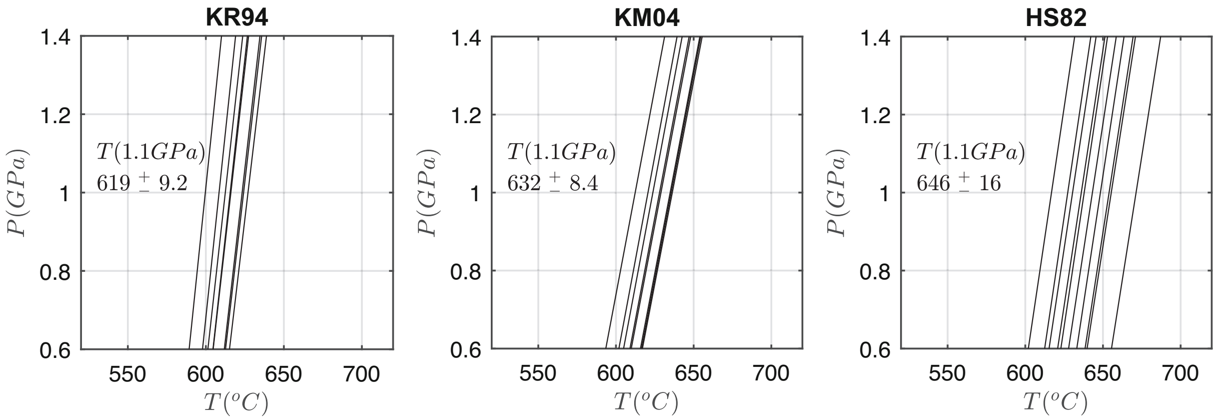

Fig. 10. Geothermometry results for garnet-biotite pairs using the formulations of Kleemann and Reinhardt, 1994; KR94), Kaneko and Miyano (2004; KM04) and Hodges and Spear (1982; HS82). Temperatures were estimated assuming a pressure of 1.1 GPa. The error indicated is the standard deviation based on the different pairs measured.

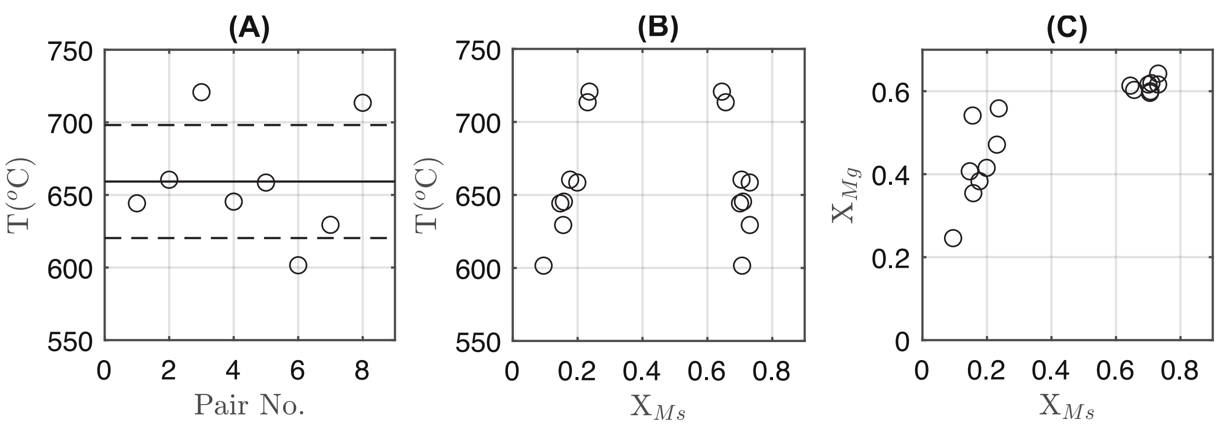

Fig. 11. Mineral chemistry and temperature estimates for coexisting white mica (muscovite-paragonite) pairs. The temperature was estimated using the formulation of Blencoe et al. (1994). (A) Two-mica solvus temperature estimates of individual pairs. The solid line indicates the mean temperature for all pairs, and the dashed lines indicate the limits of $\pm 1\ \sigma$. (B) Temperature as a function of muscovite content (X_{Ms}) in K-rich and Na-rich micas. (C) X_{Mg} [Mg/(Mg + Fe) molar ratios] of coexisting white micas as a function of their muscovite content.

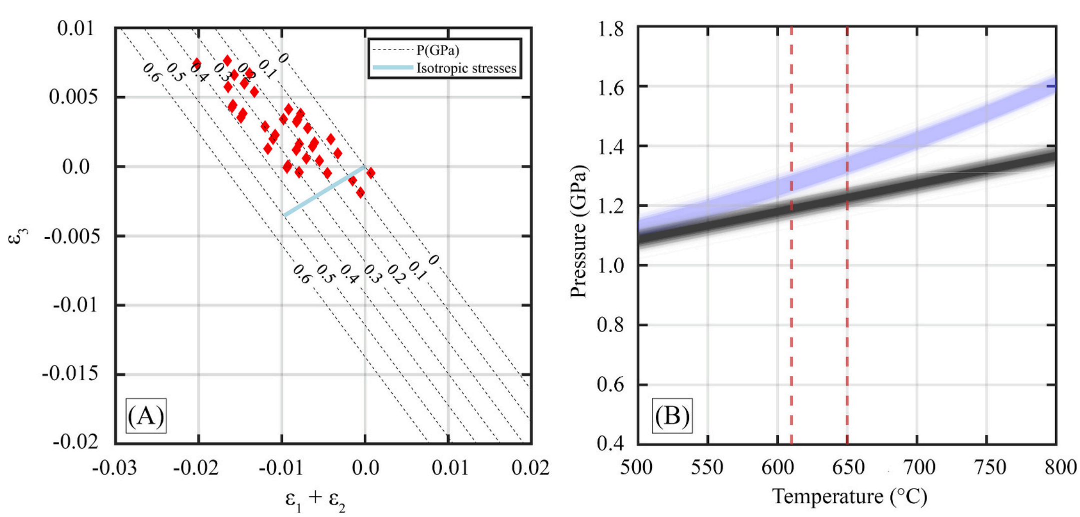

Fig. 12. Results of quartz-in-garnet elastic barometry. (A) Elastic strain components in relation to the residual pressure of quartz (contours). The blue line represents the conditions of isotropic stresses. The maximum measured residual pressure was 0.387 GPa. (B) Probability density for isomeke lines calculated based on the maximum residual pressure (0.387 GPa). The black density region represents the linear isomeke while the purple region represents the non-linear isomeke (see main text for further details). A Monte Carlo approach with 2000 iterations was used to generate the probability densities. The red dashed vertical lines indicate the approximate limits for the temperature estimates (630 ± 20 °C). (For interpretation of the references to colour in this figure legend, the reader is referred to the web version of this article.)

0.1, in excellent agreement with our determination.

As mentioned earlier, the studied sole metapelite is characterized by the presence of large K-feldspar ribbons within the matrix, as well as in localized zones and fractures associated with garnet. Our equilibrium thermodynamic calculations could not produce any field that includes K-feldspar along with the observed mineral assemblage. According to Clemens (1984, Fig.2), K-feldspar can form at relatively high temperatures (~680 °C) and very low pressures (<1 kbar) or above 700 °C at higher pressures. These findings were also supported by subsequent experimental studies (e.g., Carrington and Watt, 1995). However, such conditions indicate the onset of granulite-facies metamorphism and do not match our inferred *P-T* estimates.

Clemens (1984) also showed that K-feldspar could result from muscovite dehydration at 600–650 °C under relatively low pressures (2.6–4.6 kbar). Interestingly, K-feldspar in our sample was observed to be associated with muscovite (e.g., Fig. 3D). On another occasion, Fukuda et al. (2012) demonstrated that secondary K-feldspar can precipitate from K-rich fluids, but this process produces a fine-grained texture and requires pre-existing K-feldspar porphyroclasts. Based on the previous discussion we offer two possible explanations. The large K-feldspars could represent (a) out-of-equilibrium, dehydration products after muscovite in a later stage of the evolution of the rock, (b) remnants of a high-temperature assemblage. The presence of K-feldspar within veins in garnets, or its coexistence with plagioclase and quartz in localized regions surrounding garnets likely represents the existence of a haplogranitic melt. Our phase-equilibria models support this interpretation, predicting small degrees of partial melting under the conditions of interest (Fig. 9). Based on PERPLE_X, the melt composition at the conditions of interest spans from haplogranitic to granodioritic, with 60 wt% SiO_2, 13 wt% Al_2O_3, 7 wt% Na_2O, and 19 wt% H_2O on average.

5.2. Elastic barometry and garnet growth

In recent years, the QuiG barometer has served as a reliable tool for determining entrapment conditions based on the phonon-mode Grüneisen tensor. The accuracy of the QuiG barometer has also been demonstrated experimentally (Bonazzi et al., 2019). The application to the studied metapelitic sample indicated pressures between 1.1 and 1.3 GPa at temperatures ranging from 500 to 630 °C. These results align well with the rest of our thermobarometric estimates. The calculated pressures correspond to the possible entrapment conditions of quartz in garnet. However, it is possible that the Grüneisen tensor approach could overestimate the residual pressure by up to 0.1GPa (Fig. S9 of the supplementary material). Applying this correction would shift the isomeke lines toward lower pressures, bringing them into precise agreement with the *P–T* conditions inferred from thermobarometry. It is also noted that the inferred conditions from elastic barometry may not necessarily coincide with the chemical equilibration of the rock and could represent a distinct stage in the *P-T-t* evolution of the metapelite (Spear and Wolfe, 2020).

Zhong et al. (2020) demonstrated that the viscous relaxation of the host phase (garnet) could play a significant role in the preservation of residual pressure in quartz. At higher temperatures, the QuiG system is more prone to viscous relaxation, especially in cases where these temperatures are experienced for significant amounts of time. The process of viscous relaxation can significantly lower the pressure maintained by quartz. As a result, pressure estimates based on the isomeke concept may not reflect the original entrapment conditions, but they may rather be closer to the peak-*T* conditions. This effect has been observed, for example, in calc-silicate gneisses from the Rhodope Massif (Moulas et al., 2020). Additionally, garnet weakening and therefore pressure modification is expected in the presence of an aqueous fluid (Zhong et al., 2024). In the present work, the isomeke lines clearly indicate *P-T* conditions which coincide well with our peak thermobarometric and phase-equilibria estimates (1.1 to 1.3 GPa). Therefore, we expect that the effect of viscous relaxation is negligible beyond the inferred peak temperatures ($T < 630$ °C).

5.3. $^{40}Ar/^{39}Ar$, U—Pb ages and time constraints

$^{40}Ar/^{39}Ar$ dating is commonly discussed in the literature with respect to its closure temperature (e.g., Palandzhyan et al., 2011; Parlak and Delaloye, 1999). An $^{40}Ar/^{39}Ar$ age is usually thought to represent the "moment" where a system cooled below the closure temperature of argon for the specific mineral being analyzed (Schaen et al., 2021 and references therein). For the case of amphibole, Harrison (1982) determined Ar-closure temperatures in the range between 578 and 490 °C for variable cooling rates and assuming a monotonic cooling path. In our sample, amphibole showed a well-defined age plateau at 165.5 ± 0.73 Ma. This particular apparent age profile is a strong indication that amphibole has not been affected by diffusion or secondary alteration processes that would have led to either argon loss or gain (e.g., Jourdan, 2012 and references therein). If amphibole crystallization was immediately followed by rapid cooling, the measured $^{40}Ar/^{39}Ar$ age could reflect the actual time of formation. It is also expected that amphibole remained unaffected by any reheating events after cooling below its closure temperature (e.g., Parlak et al., 2019).

Muscovite closure temperatures proposed by Harrison et al. (2009) are largely dependent on cooling rate, grain size and pressure. For a cooling rate of 10 °C/Ma and a grain size of 100 μm, the closure temperature of Ar in muscovite at 10 kbar is 425 °C. In any case, the closure temperatures of muscovite are lower compared to those of amphibole. The investigated muscovite from the metapelite gave an apparent age of 164.16 ± 0.37 Ma but showed evidence of argon loss during the initial heating steps. Argon loss could be a result of diffusion or alteration and phase mixing processes. Since we did not observe any alteration associated with the analyzed muscovite or phase mixing with paragonite on the analyzed separate, we attribute the Ar loss to the effect of diffusion. As a consequence, this represents a partial reset of the $^{40}Ar/^{39}Ar$ age, and therefore, it is interpreted as a minimum estimate (e.g., Cassata et al., 2009).

The U—Pb analyses aimed at dating garnet growth were strongly influenced by high concentrations of U and Th. Typically, regional metamorphic garnets contain very low concentrations of U and Th (e.g., Millonig et al., 2020; Peillod et al., 2024). This suggests that our results were affected by inclusions of monazite and zircon/rutile. Walters et al. (2025) showed that such micro-inclusions can be problematic in garnet U—Pb geochronology because they may also produce well-defined regression lines. In our case, the analyses yielded a clear regression line with a lower intercept age of 178.5 ± 4.8 Ma. We consider this age unreliable because it reflects solely the inclusions. The measured age is also much older than our $^{40}Ar/^{39}Ar$ ages and may instead represent the crystallization of the inclusions. If so, these inclusions could be coeval with garnet formation. However, as Walters et al. (2025) noted, using a garnet standard to infer the age of inclusions in garnet may provide significantly inaccurate ages. For these reasons, we do not regard the U—Pb age of inclusions in garnet as robust and will exclude it from further interpretation. The accurate determination of the ages of inclusions such as monazite and zircon could provide additional insights and may be pursued in future studies.

In this study, we demonstrate a tight relationship between metamorphic sole formation (our measured $^{40}Ar/^{39}Ar$ ages) and generation of oceanic crust (gabbro U—Pb crystallization age of Liati et al., 2004) in the Pindos ophiolite. The consistent preservation of mid-Jurassic ages in the sole rocks indicates that the $^{40}Ar/^{39}Ar$ system remained unaffected by any subsequent tectono-metamorphic events or thermal resetting since the final cooling of the metamorphic sole. We notice, however, that the gabbro U—Pb age was determined by a single measurement with a high $^{207}Pb/^{206}Pb$ ratio and a large 1σ error. Therefore, it is important that the gabbros from the Pindos ophiolite are precisely redated in future work. Our new $^{40}Ar/^{39}Ar$ measurements bracket better the cooling age of magnesio-hornblende in sole amphibolites compared to previously reported data (Spray et al., 1984). Moreover, the new and accurate determinations of cooling ages for amphibole and muscovite can be used to constrain the rate of cooling from the closure temperature of amphibole (~550 °C) to that of muscovite (~400 °C). Considering the largest deviation in the ages obtained for the two minerals, based on their 2σ errors, then cooling from 550 down to 400 °C must have occurred within 2.5 Ma. These estimates are consistent with studies from the Beyşehir-Hoyran ophiolite in the Central Taurides (Parlak et al., 2019). If, on the other hand, one takes the smallest difference between the cooling ages of amphibole and muscovite then only 0.24 Ma would be required for the cooling interval. The implied cooling rate estimates exceed 60 °C/Ma in the most conservative scenario and reach up to 625 °C/Ma. However fast the cooling of the sole rocks may have been, the cooling rate must have been fast enough to prevent the viscous relaxation of quartz inclusions in garnet and to preserve the sharp chemical zonation in garnet porphyroblasts. Further investigations are needed to quantify the extend of relaxation of both the mechanical and the chemical processes in these rocks.

The cooling rates estimated for the Pindos metamorphic sole have important implications for the mechanisms active during ophiolite emplacement. Comparable rates have been calculated for the metamorphic sole of the Oman ophiolite (Hacker et al., 1996). The peak *P-T* conditions calculated in this work, together with the inferred cooling rates, are consistent with the presence of a ductile shear zone (Kiss et al., 2019). This interpretation for metamorphic soles has already been supported by several numerical studies both on the geodynamic (Duretz et al., 2016) and on the local scale (Ibragimov et al., 2024). More specifically, Ibragimov et al. (2024) reproduced the expected *T-t* path of the Oman metamorphic sole using shear-heating models, while Burg and Moulas (2022) showed that rapid cooling, similar to the one suggested for the sole rocks in our study, follows the cessation of shearing. These earlier works, along with our results, constitute strong proof that shear heating was significant (along with conductive heating) during the generation of the Pindos metamorphic sole. More recently, Garber et al. (2025) provided additional evidence for the role of shear heating in the Samail ophiolite (Oman), further strengthening this interpretation. Together with the results shown in Garber et al. (2025), our results support that shear heating may be very common during ophiolite emplacement.

5.4. Emplacement and kinematic indicators

According to tectonic plate reconstructions, from Anisian to early Norian times (240-220 Ma), the closure of the Paleo-Tethys system initiated several back-arc oceans (Stampfli and Borel, 2002). The origin of the Pindos ophiolite in Greece has been debated, with uncertainty over whether it formed in an ocean to the east (e.g., Maffione and Van Hinsbergen, 2018) or west of the Pelagonian microcontinent (Ghikas et al., 2010 and references therein). In our studied sole rocks, the rotational character of *syn*-kinematic garnet porphyroblasts (e.g., Fig. 2D) is not conclusive since different directions of shear have been deduced (although most grains show a top-to-the-NE direction). Such inconclusive data have been observed in similar rocks further north in Albania (Dimo-Lahitte et al., 2001) and can be explained by the interactions of porphyroblasts in a deforming, anisotropic rock matrix (Griera et al., 2013). By contrast, the kinematic analysis of ductile S—C structures (Fig. 2E-F) is consistent with shearing topping east, hence a westerly origin of the metamorphic-sole rocks. Rassios and Dilek (2009) have also demonstrated that the Pindos–Vourinos ophiolites have retained their relative orientations from the time of cessation of ductile deformation within the ophiolitic slab. Unless the ophiolites have been so severely dismembered and disarranged subsequent to their initial emplacement that any consistency in trends shown by fabrics and structures from within the metamorphic sole is unlikely to reflect original orientations, all macro- and microtectonic data taken together clearly support a top-to-the-NE sense of shear during emplacement of the Pindos and Vourinos ophiolites (Ghikas et al., 2010 and references therein).

6. Conclusions

Several key points emerge from the data and discussion above. Petrographic observations and thermobarometric and phase equilibria calculations for the Pindos metamorphic sole rocks, all unambiguously point to upper-amphibolite facies conditions (~630 °C and 1.1GPa) for the studied garnet-bearing metapelite. The effect of viscous relaxation on the residual pressures recorded by quartz seems to be negligible. New $^{40}Ar/^{39}Ar$ ages for muscovite (164.16 ± 0.37 Ma) and magnesio-hornblende (165.5 ± 0.73 Ma) from the metamorphic sole constrain the time of emplacement of the Pindos ophiolite and constitute evidence of rapid cooling, indicative of fast, transient processes. The preservation of mid Jurassic $^{40}Ar/^{39}Ar$ ages suggests that the system has remained undisturbed by later tectono-metamorphic events. Provided that post-emplacement deformation has not reorientated the initial ductile structures, our kinematic data suggest a westerly origin of the Pindos ophiolite.

CRediT authorship contribution statement

Dimitrios Moutzouris: Writing – original draft, Visualization, Methodology, Investigation, Formal analysis, Conceptualization. **Evangelos Moulas:** Writing – review & editing, Validation, Supervision, Methodology, Investigation, Funding acquisition, Conceptualization. **Dimitrios Kostopoulos:** Writing – review & editing, Validation, Investigation, Conceptualization. **Panagiotis Pomonis:** Writing – review & editing, Validation, Investigation, Conceptualization. **Aratz Beranoaguirre:** Writing – review & editing, Methodology. **Elias Chatzitheodoridis:** Methodology. **Axel Gerdes:** Methodology.

Funding

The authors would like to acknowledge the German Research Foundation (DFG; project number 512790090) for support related to fieldwork and analytical expenses.

Acknowledgements

This work is dedicated to the memory of Anna Kantza, an awesome friend and field companion in the Pindos Mountains and the late Dr. Annie Rassios who always was an inspiring figure and contributed greatly to the understanding of ophiolite belts in Greece and Albania. Finally, we would like to thank J. M. Garber and the second anonymous reviewer for their constructive comments.

Appendix A. Supplementary data

Supplementary data to this article can be found online at https://doi.org/10.1016/j.lithos.2025.108285.

References

Agard, P., Yamato, P., Soret, M., Prigent, C., Guillot, S., Plunder, A., Dubacq, B., Chauvet, A., Monié, P., 2016. Plate interface rheological switches during subduction infancy: control on slab penetration and metamorphic sole formation. Earth Planet. Sci. Lett. 451, 208–220.

Anders, B., Reischmann, T., Kostopoulos, D., 2007. Zircon geochronology of basement rocks from the Pelagonian Zone, Greece: Constraints on the pre-Alpine evolution of the westernmost Internal Hellenides. Int. J. Earth Sci. 96, 639–661.

Angel, R.J., Nimis, P., Mazzucchelli, M.L., Alvaro, M., Nestola, F., 2015. How large are departures from lithostatic pressure? Constraints from host–inclusion elasticity. J. Metamorph. Geol. 33, 801–813.

Angel, R.J., Murri, M., Mihailova, B., Alvaro, M., 2019. Stress, strain and Raman shifts. Zeitschrift Für Kristallographie - Crystalline Materials 234, 129–140.

Blencoe, J.G., Guidotti, C.V., Sassi, F.P., 1994. The paragonite-muscovite solvus: II. Numerical geothermometers for natural, quasibinary paragonite-muscovite pairs. Geochim. Cosmochim. Acta 58, 2277–2288.

Bonazzi, M., Tumiati, S., Thomas, J.B., Angel, R.J., Alvaro, M., 2019. Assessment of the reliability of elastic geobarometry with quartz inclusions. Lithos 350–351, 105201.
Boudier, F., Bouchez, J.L., Nicolas, A., Cannat, M., Ceuleneer, G., Misseri, M., Montigny, R., 1985. Kinematics of oceanic thrusting in the Oman ophiolite: Model of plate convergence. Earth Planet. Sci. Lett. 75, 215–222.
Burg, J.-P., Moulas, E., 2022. Cooling-rate constraints from metapelites across two inverted metamorphic sequences of the Alpine-Himalayan belt; evidence for viscous heating. J. Struct. Geol. 156, 104536.
Carrington, D.P., Watt, G.R., 1995. A geochemical and experimental study of the role of K-feldspar during water-undersaturated melting of metapelites. Chem. Geol. 122, 59–76.
Cassata, W.S., Renne, P.R., Shuster, D.L., 2009. Argon diffusion in plagioclase and implications for thermochronometry: a case study from the Bushveld complex, South Africa. Geochim. Cosmochim. Acta 73, 6600–6612.
Clemens, J.D., 1984. Water contents of silicic to intermediate magmas. Lithos 17, 273–287.
Coggon, R., Holland, T.J.B., 2002. Mixing properties of phengitic micas and revised garnet-phengite thermobarometers. J. Metamorph. Geol. 20, 683–696.
Connolly, J.A.D., 2009. The geodynamic equation of state: what and how. Geochem. Geophys. Geosyst. 10, Q10014.
Dewey, J.F., 1976. Ophiolite obduction. Tectonophysics 31, 93–120.
Dimo-Lahitte, A., Monié, P., Vergély, P., 2001. Metamorphic soles from the Albanian ophiolites: Petrology, 40Ar/39Ar geochronology, and geodynamic evolution. Tectonics 20, 78–96.
Duretz, T., Agard, P., Yamato, P., Ducassou, C., Burov, E.B., Gerya, T.V., 2016. Gondwana Res. 32, 1–10.
Enami, M., Nishiyama, T., Mouri, T., 2007. Laser Raman microspectrometry of metamorphic quartz: a simple method for comparison of metamorphic pressures. Am. Mineral. 92, 1303–1315.
Ferrière, J., Chanier, F., Reynaud, J.-Y., Pavlopoulos, A., Ditbanjong, P., Coutand, I., 2013. Evolution of the Mesohellenic Basin (Greece): a synthesis. J. Virtual Explor. 45, 1–51.
Fukuda, J., Okudaira, T., Satsukawa, T., Michibayashi, K., 2012. Solution–precipitation of K-feldspar in deformed granitoids and its relationship to the distribution of water. Tectonophysics 532–535, 175–185.
Garber, J.M., Rioux, M., Smye, A.J., Cruz-Uribe, A.M., Baker, P.L., Vervoort, J.D., Searle, M.P., Feineman, M.D., 2025. Shear heating during rapid subduction initiation beneath the Samail Ophiolite. Nat. Geosci. 18, 653–660.
Gartzos, E., Dietrich, V.J., Migiros, G., Serelis, K., Lymperopoulou, T., 2009. The origin of amphibolites from metamorphic soles beneath the ultramafic ophiolites in Evia and Lesvos (Greece) and their geotectonic implication. Lithos 108, 224–242.
Ghikas, C., Dilek, Y., Rassios, A.E., 2010. Structure and tectonics of subophiolitic mélanges in the western Hellenides (Greece): Implications for ophiolite emplacement tectonics. Int. Geol. Rev. 52, 423–453.
Green, T.H., Hellman, P.L., 1982. Fe-Mg partitioning between coexisting garnet and phengite te at high pressure, and comments on a garnet-phengite geothermometer. Lithos 15, 253–266.
Green, E.C.R., White, R.W., Diener, J.F.A., Powell, R., Holland, T.J.B., Palin, R.M., 2016. Activity–composition relations for the calculation of partial melting equilibria in metabasic rocks. J. Metamorph. Geol. 34, 845–869.
Griera, A., Llorens, M.-G., Gomez-Rivas, E., Bons, P.D., Jessell, M.W., Evans, L.A., Lebensohn, R., 2013. Numerical modelling of porphyroclast and porphyroblast rotation in anisotropic rocks. Deformation, Pophyroblasts and Mountain Building: A Special Issue in Honor of the Career Contributions of T.H. Bell Tectonophysics 587, 4–29.
Hacker, B.R., Mosenfelder, J.L., Gnos, E., 1996. Rapid emplacement of the Oman ophiolite: thermal and geochronologic constraints. Tectonics 15, 1230–1247.
Harrison, T.M., 1982. Diffusion of 40Ar in hornblende. Contrib. Mineral. Petrol. 78, 324–331.
Harrison, T.M., Célérier, J., Aikman, A.B., Hermann, J., Heizler, M.T., 2009. Diffusion of 40Ar in muscovite. Geochim. Cosmochim. Acta 73, 1039–1051.
Hawthorne, F.C., Oberti, R., Harlow, G.E., Maresch, W.V., Martin, R.F., Schumacher, J. C., Welch, M.D., 2012. Nomenclature of the amphibole supergroup. Am. Mineral. 97, 2031–2048.
Hodges, K.V., Spear, F.S., 1982. Geothermometry, geobarometry and the Al2SiO5 triple point at Mt. Moosilauke, New Hampshire. Am. Mineral. 67, 1118–1134.
Holland, T.J.B., Powell, R., 1998. An internally consistent thermodynamic data set for phases of petrological interest. J. Metamorph. Geol. 16, 309–343.
Holland, T.J.B., Powell, R., 2011. An improved and extended internally consistent thermodynamic dataset for phases of petrological interest, involving a new equation of state for solids. J. Metamorph. Geol. 29, 333–383.
Hunziker, D., Burg, J.-P., Moulas, E., Reusser, E., Omrani, J., 2017. Formation and preservation of fresh lawsonite: Geothermobarometry of the North Makran Blueschists, Southeast Iran. J. Metamorph. Geol. 35, 871–895.
Ibragimov, I., Kiss, D., Moulas, E., 2024. A thermo-mechanical model of the thermal evolution and incorporation of metamorphic soles in Tethyan ophiolites: a case study from Oman. Austrian J. Earth Sci. 117, 13–24.
Jones, G., Robertson, A.H.F., 1991. Tectono-stratigraphy and evolution of the Mesozoic Pindos ophiolite and related units, northwestern Greece. J. Geol. Soc. Lond. 148, 267.
Jones, G., De Wever, P., Robertson, A.H.F., 1992. Significance of radiolarian age data to the Mesozoic tectonic and sedimentary evolution of the northern Pindos Mountains, Greece. Geol. Mag. 129, 385–400.
Jourdan, F., 2012. The $^{40}Ar/^{39}Ar$ dating technique applied to planetary sciences and terrestrial impacts. Aust. J. Earth Sci. 59, 199–224.
Kaneko, Y., Miyano, T., 2004. Recalibration of mutually consistent garnet–biotite and garnet–cordierite geothermometers. Lithos 73, 255–269.
Kemp, A.E.S., McCaig, A.M., 1984. Origins and significance of rocks in an imbricate thrust zone beneath the Pindos ophiolite, northwestern Greece. Geol. Soc. Lond. Spec. Publ. 17, 569–580.
Kiss, D., Podladchikov, Y., Duretz, T., Schmalholz, S.M., 2019. Spontaneous generation of ductile shear zones by thermal softening: Localization criterion, 1D to 3D modelling and application to the lithosphere. Earth Planet. Sci. Lett. 519, 284–296.
Kleemann, U., Reinhardt, J., 1994. Garnet-biotite thermometry revisited: the effect of AlVI and Ti in biotite. Eur. J. Mineral. 6, 925–942.
Kostopoulos, D.K., 1989. Geochemistry, Petrogenesis and Tectonic Setting of the Pindos Ophiolite. NW Greece. Newcastle upon Tyne.
Liati, A., Gebauer, D., Fanning, C.M., 2004. The age of ophiolitic rocks of the Hellenides (Vourinos, Pindos, Crete): First U–Pb ion microprobe (SHRIMP) zircon ages. Chem. Geol. 207, 171–188.
Locock, A.J., 2014. An Excel spreadsheet to classify chemical analyses of amphiboles following the IMA 2012 recommendations. Comput. Geosci. 62, 1–11.
Maffione, M., Van Hinsbergen, D.J.J., 2018. Reconstructing Plate Boundaries in the Jurassic Neo-Tethys from the East and West Vardar Ophiolites (Greece and Serbia). Tectonics 37, 858–887.
Millonig, L.J., Albert, R., Gerdes, A., Avigad, D., Dietsch, C., 2020. Exploring laser ablation U–Pb dating of regional metamorphic garnet – The Straits Schist, Connecticut, USA. Earth Planet. Sci. Lett. 552, 116589.
Moulas, E., Kostopoulos, D., Podladchikov, Y., Chatzitheodoridis, E., Schenker, F.L., Zingerman, K.M., Pomonis, P., Tajčmanová, L., 2020. Calculating pressure with elastic geobarometry: a comparison of different elastic solutions with application to a calc-silicate gneiss from the Rhodope Metamorphic Province. Lithos 378–379, 105803.
Moulas, E., Podladchikov, Y., Zingerman, K., Vershinin, A., Levin, V., 2023. Large-strain Elastic and Elasto-Plastic Formulations for Host-Inclusion Systems and their applications in Thermobarometry and Geodynamics. Am. J. Sci. 323, 2.
Myhill, R., 2011. Constraints on the evolution of the Mesohellenic Ophiolite from subophiolitic metamorphic rocks. Geol. Soc. Am. Spec. Pap. 480, 75–94.
Nerone, S., Lanari, P., Dominguez, H., Forshaw, J.B., Groppo, C., Rolfo, F., 2025. IntersecT: a Python script for quantitative isopleth thermobarometry of equilibrium and disequilibrium systems. Comput. Geosci. 202, 105949.
Palandzhyan, S.A., Layer, P.W., Patton, W.W., Khanchuk, A.I., 2011. Geodynamic interpretation of the 40Ar/39Ar dating of ophiolitic and arc-related mafics and metamafics of the northern part of the Anadyr-Koryak region. Geotectonics 45, 481–495.
Parlak, O., Delaloye, M., 1999. Precise 40Ar/39Ar ages from the metamorphic sole of the Mersin ophiolite (southern Turkey). Tectonophysics 301, 145–158.
Parlak, O., Dunkl, I., Karaoğlan, F., Kusky, T.M., Zhang, C., Wang, L., Koepke, J., Billor, Z., Hames, W.E., Şimşek, E., Şimşek, G., Şimşek, T., Öztürk, S.E., 2019. Rapid cooling history of a Neotethyan ophiolite: evidence for contemporaneous subduction initiation and metamorphic sole formation. Geol. Soc. Am. Bull. 131, 2011–2038.
Peillod, A., Patten, C.G.C., Drüppel, K., Beranoaguirre, A., Zeh, A., Gudelius, D., Hector, S., Majka, J., Kleine-Marshall, B.I., Karlson, A., Gerdes, A., Kolb, J., 2024. Disruption of a high-pressure unit during exhumation: example of the Cycladic Blueschist unit (Thera, Ios and Naxos islands, Greece). J. Metamorph. Geol. 42, 225–255.
Pomonis, P., Tsikouras, B., Hatzipanagiotou, K., 2002. Origin, evolution and radiometric dating of subophiolitic metamorphic rocks from the Koziakas ophiolite (W. Thessaly, Greece). Neues Jahrbuch Für Mineralogie, Abhandlungen 177, 255–276.
Rassios, A., Dilek, Y., 2009. Rotational deformation in the Jurassic Mesohellenic ophiolites, Greece, and its tectonic significance. Lithos 108, 207–223.
Rassios, A., Moores, E.M., 2006. Heterogeneous mantle complex, crustal processes, and obduction kinematics in a unified Pindos-Vourinos ophiolitic slab (northern Greece). Geol. Soc. Lond. Spec. Publ. 260, 237–266.
Rassios, A., Smith, A.G., Kostopoulos, D.K., 2009. Ophiolites 2008 guidebook: link between the Mesohellenic Ophiolites and Pelagonian margin. J. Virtual Explor. 34.
Robertson, A., 2004. Development of concepts concerning the genesis and emplacement of Tethyan ophiolites in the Eastern Mediterranean and Oman regions. Earth Sci. Rev. 66, 331–387.
Robertson, A.H.F., Clift, P.D., Degnan, P.J., Jones, G., 1991. Palaeogeographic and palaeotectonic evolution of the Eastern Mediterranean Neotethys. Palaeogeogr. Palaeoclimatol. Palaeoecol. 87, 289–343.
Schaen, A.J., Jicha, B.R., Hodges, K.V., Vermeesch, P., Stelten, M.E., Mercer, C.M., Phillips, D., Rivera, T.A., Jourdan, F., Matchan, E.L., Hemming, S.R., Morgan, L.E., Kelley, S.P., Cassata, W.S., Heizler, M.T., Vasconcelos, P.M., Benowitz, J.A., Koppers, A.A.P., Mark, D.F., Singer, B.S., 2021. Interpreting and reporting 40Ar/39Ar geochronologic data. Geol. Soc. Am. Bull. 133, 461–487.
Sergeev, D.S., Dijkstra, A.H., Meisel, T., Brügmann, G., Sergeev, S.A., 2014. Traces of ancient mafic layers in the Tethys oceanic mantle. Earth Planet. Sci. Lett. 389, 155–166.
Siivola, J., Schmid, R., 2007. Recommendations by the IUGS Subcommission on the Systematics of Metamorphic Rocks: List of mineral abbreviations..
Smith, A.G., 1993. Tectonic significance of the Hellenic-Dinaric ophiolites. Geol. Soc. Lond. Spec. Publ. 76, 213–243.
Smith, A.G., Spray, J.G., 1984. A half-ridge transform model for the Hellenic-Dinaric ophiolites. Geol. Soc. Lond. Spec. Publ. 17, 629–644.
Smith, A.G., Woodcock, N.H., Naylor, M.A., 1979. The structural evolution of a Mesozoic continental margin, Othris Mountains, Greece. J. Geol. Soc. Lond. 136, 589–601.
Spear, F.S., Wolfe, O.M., 2020. Revaluation of "equilibrium" P-T paths from zoned garnet in light of quartz inclusion in garnet (QuiG) barometry. Lithos 372–373, 105650.

Spray, J.G., 1984. Possible causes and consequences of upper mantle decoupling and ophiolite displacement. Geol. Soc. Lond. Spec. Publ. 13, 255.
Spray, J.G., Bébien, J., Rex, D.C., Roddick, J.C., 1984. Age constraints on the igneous and metamorphic evolution of the Hellenic-Dinaric ophiolites. Geol. Soc. Lond. Spec. Publ. 17, 619.
Stampfli, G.M., Borel, G.D., 2002. A plate tectonic model for the Paleozoic and Mesozoic constrained by dynamic plate boundaries and restored synthetic oceanic isochrons. Earth Planet. Sci. Lett. 196 (1–2), 17–33. https://doi.org/10.1016/S0012-821X(01)00588-X.
Stampfli, G.M., Hochard, C., Vérard, C., Wilhem, C., von Raumer, J., 2013. The formation of Pangea. Tectonophysics 593, 1–19.
Tinkham, D.K., Zuluaga, C.A., Stowell, H.H., 2001. Metapelite phase equilibria modeling in MnNCKFMASH: the effect of variable Al2O3 and MgO/(MgO+FeO) on mineral stability. Geol. Mater. Res. 3, 1–42.
Walters, J.B., Garber, J.M., Beranoaguirre, A., Millonig, L., Gerdes, A., Grützner, T., Marschall, H.R., 2025. Zircon micro-Inclusions as an Obstacle for In Situ Garnet U-Pb Geochronology: An Example from the as Sifah Eclogite Locality. EGUsphere, preprint, Oman.
Weinberg, R.F., Hasalová, P., 2015. Water-fluxed melting of the continental crust: a review. Lithos 212–215, 158–188.
Wijbrans, J.R., McDougall, I., 1988. Metamorphic evolution of the attic Cycladic Metamorphic Belt on Naxos (Cyclades, Greece) utilizing ^{40}Ar/^{39}Ar age spectrum measurements. J. Metamorph. Geol. 6, 571–594.
Williams, H., Smyth, W.R., 1973. Metamorphic aureoles beneath ophiolite suites and alpine peridotites; tectonic implications with West Newfoundland examples. Am. J. Sci. 273, 594–621.
Wu, C.-M., Zhao, G., 2006. Recalibration of the Garnet–Muscovite (GM) Geothermometer and the Garnet–Muscovite–Plagioclase–Quartz (GMPQ) Geobarometer for Metapelitic Assemblages. J. Petrol. 47, 2357–2368.
Zhong, X., Moulas, E., Tajčmanová, L., 2020. Post-entrapment modification of residual inclusion pressure and its implications for Raman elastic thermobarometry. Solid Earth 11, 223–240.
Zhong, X., Wallis, D., Kingsbery, P., John, T., 2024. The effect of aqueous fluid on viscous relaxation of garnet and modification of inclusion pressures after entrapment. Earth Planet. Sci. Lett. 636, 118713.